



Publication Year	2019
Acceptance in OA @INAF	2020-12-30T17:00:17Z
Title	Chandra Spectral and Timing Analysis of Sgr A*'s Brightest X-Ray Flares
Authors	Haggard, Daryl; Nynka, Melania; Mon, Brayden; de la Cruz Hernandez, Noelia; Nowak, Michael; et al.
DOI	10.3847/1538-4357/ab4a7f
Handle	http://hdl.handle.net/20.500.12386/29399
Journal	THE ASTROPHYSICAL JOURNAL
Number	886



Chandra Spectral and Timing Analysis of Sgr A*'s Brightest X-Ray Flares

Daryl Haggard^{1,2,3}, Melania Nynka^{1,2,4}, Brayden Mon^{1,2}, Noelia de la Cruz Hernandez^{1,2}, Michael Nowak⁵, Craig Heinke⁶, Joseph Neilsen⁷, Jason Dexter^{8,9}, P. Chris Fragile¹⁰, Fred Baganoff⁴, Geoffrey C. Bower¹¹, Lia R. Corrales¹², Francesco Coti Zelati^{13,14}, Nathalie Degenaar¹⁵, Sera Markoff^{15,16}, Mark R. Morris¹⁷, Gabriele Ponti^{8,18}, Nanda Rea^{13,14}, Jörn Wilms¹⁹, and Farhad Yusef-Zadeh²⁰

¹ Department of Physics, McGill University, 3600 University Street, Montréal, QC H3A 2T8, Canada; daryl.haggard@mcgill.ca

² McGill Space Institute, McGill University, 3550 University Street, Montréal, QC H3A 2A7, Canada

³ CIFAR Azrieli Global Scholar, Gravity & the Extreme Universe Program, Canadian Institute for Advanced Research, 661 University Avenue, Suite 505, Toronto, ON M5G 1M1, Canada

⁴ MIT Kavli Institute for Astrophysics and Space Research, 77 Massachusetts Avenue, Cambridge, MA 02139, USA

⁵ Department of Physics, Washington University, 1 Brookings Drive, St. Louis, MO 63130, USA

⁶ Department of Physics, University of Alberta, CCIS 4-183, Edmonton AB T6G 2E1, Canada

⁷ Department of Physics, Villanova University, 800 Lancaster Avenue, Villanova, PA 19085, USA

⁸ Max-Planck-Institut für Extraterrestrische Physik, Giessenbachstrasse, D-85748 Garching, Germany

⁹ JILA and Department of Astrophysical and Planetary Sciences, University of Colorado, Boulder, CO 80309, USA

¹⁰ Department of Physics and Astronomy, College of Charleston, Charleston, SC 29424, USA

¹¹ Academia Sinica Institute of Astronomy and Astrophysics, 645 N. A'ohoku Place, Hilo, HI 96720, USA

¹² Department of Astronomy, University of Michigan, 1085 S. University, Ann Arbor, MI 48109, USA

¹³ Institut de Space Sciences (CSIC), Campus UAB, Carrer de Can Magrans s/n, E-08193 Barcelona, Spain

¹⁴ Institut d'Estudis Espacials de Catalunya (IEEC), E-08034 Barcelona, Spain

¹⁵ Anton Pannekoek Institute for Astronomy, University of Amsterdam, Science Park 904, NL-1098 XH Amsterdam, The Netherlands

¹⁶ Gravitational and Astroparticle Physics Amsterdam, U. Amsterdam, Science Park 904, NL-1098 XH Amsterdam, The Netherlands

¹⁷ University of California, Los Angeles, CA 90095, USA

¹⁸ Osservatorio Astronomico di Brera, Via E. Bianchi 46, I-23807 Merate (LC), Italy

¹⁹ Dr. Karl-Reemis-Sternwarte and Erlangen Centre for Astroparticle Physics, Sternwartstr. 7, D-96049, Bamberg, Germany

²⁰ Department of Physics and Astronomy and Center for Interdisciplinary Exploration and Research in Astrophysics (CIERA), Northwestern University, Evanston, IL 60208, USA

Received 2018 December 21; revised 2019 September 30; accepted 2019 October 1; published 2019 November 25

Abstract

We analyze the two brightest *Chandra* X-ray flares detected from Sagittarius A*, with peak luminosities more than 600× and 245× greater than the quiescent X-ray emission. The brightest flare has a distinctive double-peaked morphology—it lasts 5.7 ks (~2 hr), with a rapid rise time of 1500 s and a decay time of 2500 s. The second flare lasts 3.4 ks, with rise and decay times of 1700 and 1400 s. These luminous flares are significantly harder than quiescence: the first has a power-law spectral index $\Gamma = 2.06 \pm 0.14$ and the second has $\Gamma = 2.03 \pm 0.27$, compared to $\Gamma = 3.0 \pm 0.2$ for the quiescent accretion flow. These spectral indices (as well as the flare hardness ratios) are consistent with previously detected Sgr A* flares, suggesting that bright and faint flares arise from similar physical processes. Leveraging the brightest flare's long duration and high signal-to-noise, we search for intraflare variability and detect excess X-ray power at a frequency of $\nu \approx 3$ mHz, but show that it is an instrumental artifact and not of astrophysical origin. We find no other evidence (at the 95% confidence level) for periodic or quasi-periodic variability in either flares' time series. We also search for nonperiodic excess power but do not find compelling evidence in the power spectrum. Bright flares like these remain our most promising avenue for identifying Sgr A*'s short timescale variability in the X-ray, which may probe the characteristic size scale for the X-ray emission region.

Key words: accretion, accretion disks – black hole physics – Galaxy: center – radiation mechanisms: non-thermal – X-rays: individual (Sgr A*)

1. Introduction

Near-infrared observations of massive stars orbiting Sagittarius A* (Sgr A*), the supermassive black hole (SMBH) at the Milky Way's center, have yielded precise measurements of its mass and distance, $(4.28 \pm 0.1) \times 10^6 M_\odot$ and 7.97 ± 0.07 kpc (e.g., Ghez et al. 2008; Gillessen et al. 2009, 2017; Boehle et al. 2016; Gravity Collaboration et al. 2018b, 2019; Do et al. 2019). *Chandra* X-ray observations have revealed Sgr A* as a compact (~1"), low-luminosity source ($L_{2-10 \text{ keV}} \sim 2 \times 10^{33} \text{ erg s}^{-1}$), with a very low Eddington ratio, $L/L_{\text{Edd}} \sim 10^{-8}$ to 10^{-11} (Figure 1; e.g., Baganoff et al. 2001, 2003; Xu et al. 2006; Genzel et al. 2010; Wang et al. 2013). The size of the X-ray emitting region is similar to the black hole's Bondi radius (~6000 au, roughly 10^5 times the Schwarzschild radius),

through which the accretion rate is $10^{-6} M_\odot \text{ yr}^{-1}$ (Melia 1992; Quataert 2002). The gas reservoir likely originates from captured winds from the S stars or the cluster of massive OB stars surrounding Sgr A* (Cuadra et al. 2005, 2006, 2008; Yusef-Zadeh et al. 2016; Russell et al. 2017), only a fraction of which reaches the SMBH—the vast majority of the material is apparently ejected in an outflow (e.g., Wang et al. 2013).

Ambitious X-ray campaigns with *Chandra*, *XMM-Newton*, *Swift*, and *NuSTAR* have targeted Sgr A* and shown that its emission is relatively quiescent and has been stable over two decades, punctuated by approximately daily X-ray flares (Baganoff et al. 2001; Goldwurm et al. 2003; Porquet et al. 2003, 2008; Bélanger et al. 2005; Nowak et al. 2012; Degenaar et al. 2013; Neilsen et al. 2013, 2015; Barrière et al. 2014;

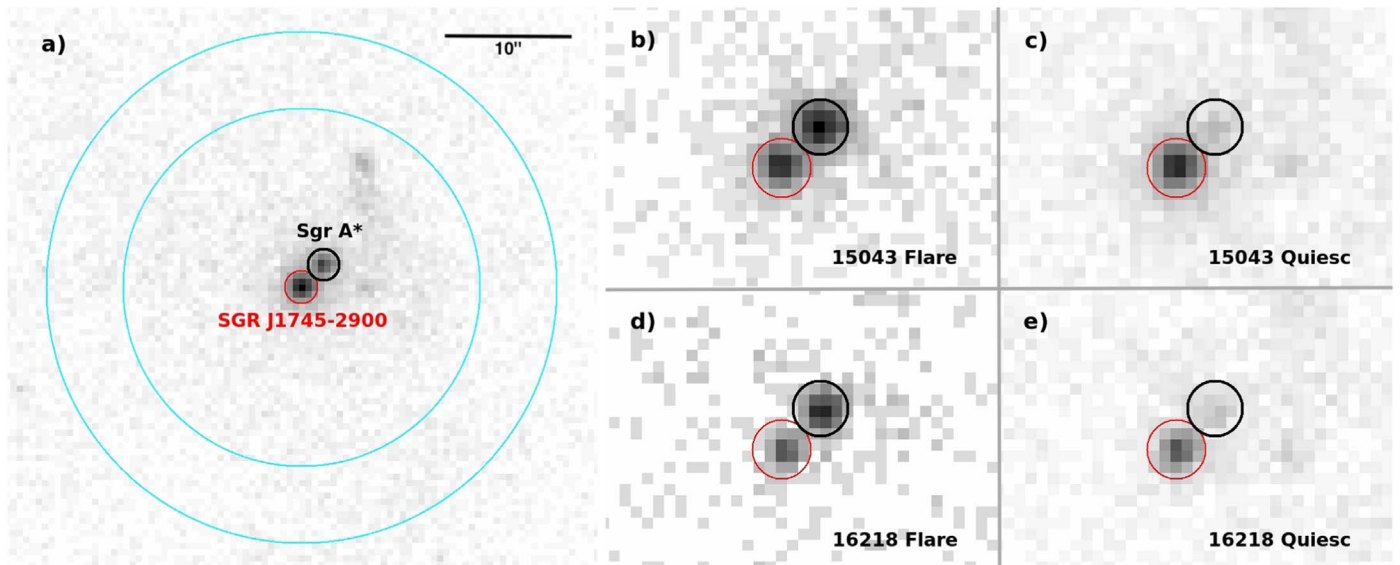


Figure 1. *Chandra* X-ray images of Sgr A* and the magnetar, SGR J1745–2900, on a logarithmic scale in the 2–8 keV band. Two bright X-ray flares from Sgr A* are clearly visible, as is the decay of the magnetar’s flux between 2013 September 14 (ObsID 15043) and 2014 October 20 (ObsID 16218). The large panel (a) shows the full 45.41 ks exposure for ObsID 15043—extraction regions for Sgr A* ($\sim 1''.25$ radius) and the magnetar ($1''.3$ radius) are shown as black and red circles, respectively, and the background region (matched to the SGR J1745–2900 analysis of Coti Zelati et al. 2017) is marked with a cyan annulus. Smaller panels show the flare and quiescent intervals for ObsID 15043 (b, c) and ObsID 16218 (d, e). The duration of the quiescent periods exceed the flare durations (Table 2), so the quiescent images have been rescaled by their exposure time to match the contrast in the flare images.

Ponti et al. 2015; Mossoux et al. 2016; Yuan & Wang 2016; Zhang et al. 2017; Bouffard et al. 2019). The quiescent component is well-modeled by bremsstrahlung emission from a hot plasma with temperature $T \sim 7 \times 10^7$ K and electron density $n_e \sim 100 \text{ cm}^{-3}$ located near the Bondi radius (Quataert 2002; Wang et al. 2013).

Baganoff et al. (2001) identified the first Sgr A* X-ray flare with *Chandra* and modeled it using a power-law spectrum with $\Gamma = 1.3_{-0.6}^{+0.5}$ and $N_H = 4.6 \times 10^{22} \text{ cm}^{-2}$, but pile-up led to known biases in the analysis. X-ray flares were subsequently observed by *XMM-Newton* (Goldwurm et al. 2003; Porquet et al. 2003, 2008; Bélanger et al. 2005; Ponti et al. 2015; Mossoux et al. 2016; Mossoux & Grosso 2017) for which pile-up is less severe, and *Swift* (e.g., Degenaar et al. 2013), establishing X-ray flares as an important emission mechanism.

These findings motivated the *Chandra* Sgr A* X-ray Visionary Program²¹ (XVP) in 2012, which utilized the high energy transmission gratings (HETG) to achieve high spatial and spectral resolution, and to avoid complications from pile-up. The XVP uncovered a very bright flare reported by Nowak et al. (2012), and provided a large, uniform sample of fainter flares (Nielsen et al. 2013, 2015). *NuSTAR* observations have since confirmed that Sgr A*’s X-ray flares can have counterparts at even higher energies (up to ~ 79 keV; Barrière et al. 2014; Zhang et al. 2017).

Detection of large numbers of X-ray flares has allowed us to establish correlations between the flare durations, fluences, and peak luminosities (Nielsen et al. 2013, 2015). However, the physical processes driving the flares are still up for debate. Magnetic reconnection is a favored energy injection mechanism and can explain the trends, but current observations cannot rule out tidal disruption of \sim kilometer-sized rocky bodies (Čadež et al. 2008; Kostić et al. 2009; Zubovas et al. 2012), stochastic acceleration, shocks from jets or accretion flow dynamics, or

even gravitational lensing of hot spots in the accretion flow (e.g., recent efforts by Dibi et al. 2014, 2016; Ball et al. 2016, 2018; Karssen et al. 2017; Gravity Collaboration et al. 2018a). The radiation mechanisms are also debated, though synchrotron radiation is favored, particularly in recent joint X-ray and near-infrared (NIR) studies (e.g., Ponti et al. 2017; Zhang et al. 2017; Fazio et al. 2018; Boyce et al. 2019).

X-ray monitoring of Sgr A* continued post-XVP, targeting the pericenter passage of the enigmatic object “G2” (e.g., Gillessen et al. 2012; Plewa et al. 2017; Witzel et al. 2017). These surveys captured the first outburst from the magnetar SGR J1745–2900, separated from Sgr A* by only $2''.4$ (Figure 1; Kennea et al. 2013; Mori et al. 2013; Rea et al. 2013; Coti Zelati et al. 2015, 2017)—this bright source complicated X-ray monitoring for all but the *Chandra* X-ray Observatory, whose spatial resolution is sufficient to disentangle it from Sgr A*.

We present an analysis of two of Sgr A*’s brightest X-ray flares, discovered during the 2013–2014 post-XVP *Chandra* campaigns. In Section 2 we describe the *Chandra* X-ray observations, in Sections 3–5 we present the X-ray lightcurves, spectral models, and power spectra of these two spectacular events. We discuss our findings in Section 6 and conclude briefly in Section 7.

2. Observations

We report two extremely bright X-ray flares from Sgr A* discovered during *Chandra* ObsID 15043 on 2013 September 14 (F1) and ObsID 16218 on 2014 October 20 (F2). The observations and quiescent and flare characteristics are summarized in Tables 1 and 2, and visualized in Figures 1 and 2. Observations were acquired using the ACIS-S3 chip in FAINT mode with a $1/8$ subarray. The small subarray helps mitigate photon pile-up, and achieves a frame rate of 0.44 s (versus *Chandra*’s standard rate of 3.2 s).

²¹ Sgr A* *Chandra* XVP: <http://www.sgra-star.com/>.

Table 1
Chandra Sgr A* Quiescent Properties

ObsID	Start (MJD)	Stop (MJD)	Mean (cnts/s)	Variance (cnts/s)
15043	56549.22	56549.59	9.4×10^{-3}	0.9×10^{-3}
16218	56950.36 56950.67	56950.49 56950.82	5.9×10^{-3}	0.6×10^{-3}

Note. GTIs for the quiescent intervals in ObsID 15043 and 16218, and the corresponding mean and variance in the quiescent count rate. Flare properties are detailed in Table 2.

Chandra data reduction and analysis are performed with CIAO v.4.8 tools (CALDB v4.7.2; Fruscione et al. 2006). We reprocess the level 2 event files, apply the latest calibrations with the *Chandra* repro script, and extract the 2–8 keV lightcurves, as well as X-ray spectra, from a circular region with a radius of $1''.25$ (2.5 pixels; Figure 1) centered on the radio position of Sgr A*: R.A. = 17:45:40.0409, decl. = $-29:00:28.118$ (J2000.0; Reid & Brunthaler 2004). The small extraction region and energy filter help isolate the flare emission from Sgr A* and minimize contamination from diffuse X-ray background emission (e.g., Nowak et al. 2012; Neilsen et al. 2013). Lightcurves and spectra from the magnetar SGR J1745–2900 are also extracted from a circular aperture with radius = $1''.3$ (Figures 1 and 2; see also Coti Zelati et al. 2015, 2017).

3. Lightcurves

We present lightcurves from Sgr A* and the magnetar SGR J1745–2900 during two bright Sgr A* X-ray flares in Figure 2. The top panels show the flares with 300 s binning, with an additional ~ 20 ks before and after the outbursts—the full data sets are roughly double this length (Table 2) but do not contain additional flares. Sgr A*'s 2–8 keV emission is shown in black; the blue and green curves represent the 4–8 keV and 2–4 keV lightcurves, respectively. Though each Sgr A* observation shows stable quiescent emission punctuated by a long, high contrast flare, the 2–8 keV lightcurve from the magnetar SGR J1745–2900 (orange curve) does not indicate variability during these epochs. Hence we attribute the flare emission to the SMBH alone.

To determine the mean and variance of the quiescent count rates in nonflare intervals, we define quiescent good time intervals (GTIs) separated by ~ 6 ks from the flares, shown in Table 1. The quiescent GTIs amount to 29.5 ks and 22.4 ks of exposure for ObsID 16218 and 15043, respectively. For flare F2 we also exclude the secondary flare at ~ 56950.63 MJD. The gray shaded regions in Figure 2 represent unused intervals not included in either the flare or quiescent GTIs. We define the flare start and stop times as those points where the count rate rises 2σ above the quiescent mean (marked with the first and last cyan points in the top panels of Figure 2).

Ponti et al. (2015) calculated the relationship between the incident 2–8 keV count rate and the observed count rate for the *Chandra* ACIS-S detectors and found that pile-up produces detected count rates up to $\sim 90\%$ lower than they should be, even in the $1/8$ subarray mode. We use their relation to compensate for the effects of pile-up (see Section 3.5) and

report the fluence, mean, and max count rates for the raw and corrected lightcurves in Table 2.

3.1. F1: 2013 September 14

F1 is the brightest Sgr A* X-ray flare yet detected by *Chandra* (Figure 2, left panels). It has a double-peaked morphology with a rapid rise and a slight shoulder in the decline. The rise time of 1500 s is measured from the start of the flare to the maximum of the first peak (first two cyan points; first peak occurs at 56549.10 MJD). The decay time of 2500 s is measured from the maximum of the second peak to the end of the flare (second two cyan points; second peak at 56549.12 MJD). The entire flare lasts 5.7 ks (approximately 2 hr), and the two bright peaks are separated by 1.8 ks (~ 30 minutes).

F1 has a mean raw count rate of 0.48 ± 0.01 counts s^{-1} , determined by averaging photons within the flare-only GTI, compared to the mean quiescent count rate of 0.009 ± 0.01 counts s^{-1} . The two individual sub-peaks reach their maxima at 1.04 ± 0.06 and 0.93 ± 0.06 counts s^{-1} , or a factor of 2.2 ± 0.1 and 1.9 ± 0.1 times the average flare-only count rate, respectively. (These are raw count rates, pile-up-corrected count rates are listed in Table 2 and discussed further in Section 3.5.)

3.2. F2: 2014 October 20

F2 is a factor of ~ 2.5 less luminous than F1, and yet is the second-brightest Sgr A* *Chandra* X-ray flare reported (Figure 2, right panels). This flare also has complex morphology, though it does not show the distinctive double-peaked structure seen in F1 (peak occurs at 56950.58 MJD). There is a small shoulder during its rise (which may be a precursor flare or a substructure), after which it smoothly peaks and decays back to quiescence. The flare lasts approximately 3.4 ks (~ 1 hr) and its morphology is similar to the bright flare reported by Nowak et al. (2012). The maximum F2 flare raw count rate of 0.52 ± 0.04 counts s^{-1} is a factor of 2.4 ± 0.2 times its raw mean count rate of 0.22 ± 0.01 counts s^{-1} . The mean quiescent count rate is 0.006 ± 0.01 counts s^{-1} . Approximately 2 ks after the end of the bright flare we detect another, smaller peak, rising $\sim 4\times$ above the mean quiescent level.

3.3. Lightcurve Morphologies

The lightcurve models and best fit parameters for F1 and F2 are described in detail in Appendix B; we summarize them here. The model for F1 is composed of four symmetric Gaussians: one for each of the two tall peaks, one for the last small subpeak, and one to model the asymmetry in the rise and decay. The model for the F2 lightcurve has two components: a symmetric Gaussian representing the main flare and a skewed Gaussian to model the preflare shoulder. The F2 fit also includes a third skewed Gaussian to model the small secondary flare near ~ 56950.63 MJD. Both models contain a constant component for the quiescent contribution. Since the hardness ratios are relatively constant (Section 3.4), we fit these 2–8 keV models to the 2–4 keV and 4–8 keV lightcurves as well. The best-fit, composite models are shown as solid red lines in the top panels of Figure 2 and Figure 3.

Table 2
Chandra Sgr A* Bright Flare Properties

Timing											
Flare	ObsID	Tot Exp (ks)	Flare Start (MJD)	Flare Stop (MJD)	Flare Duration (ks)	Rise Time (s)	Decay Time (s)	Fluence raw/corr (cnts)	Mean Rate raw/corr (cnts/s)	Peak1 Rate raw/corr (cnts/s)	Peak2 Rate raw/corr (cnts/s)
F1	15043	45.41	56549.08	56549.15	5.73	1500	2500	2769/3115	0.48/0.54	1.04/1.17	0.93/1.06
F2	16218	36.35	56950.56	56950.60	3.36	1700	1400	734/825	0.22/0.24	0.52/0.59	...
Spectral Fits											
Flare	State	Flare					Magnetar				
		F_{2-8}^{abs}	F_{2-8}^{unabs} ($\times 10^{-12}$ erg cm $^{-2}$ s $^{-1}$)	F_{2-10}^{unabs}	L_{2-10}^{unabs} ($\times 10^{34}$ erg s $^{-1}$)	Γ	HR	$F_{2-8}^{\text{abs}} \times 10^{-12}$ (erg cm $^{-2}$ s $^{-1}$)	kT (keV)	α	χ^2/DoF
F1	Mean	28.5 $^{+1.7}_{-1.6}$	64.8 $^{+3.2}_{-3.1}$	74.4 $^{+3.7}_{-3.5}$	57.0 $^{+2.8}_{-2.7}$	2.06 \pm 0.14	1.7 \pm 0.3	6.9 \pm 0.2	0.79 \pm 0.02	0.68 $^{+0.19}_{-0.17}$	514.5/423
F1	Peak1	61.3 $^{+1.7}_{-1.6}$	139.5 $^{+3.2}_{-3.1}$	160.1 $^{+3.7}_{-3.5}$	122.6 $^{+2.8}_{-2.7}$
F1	Peak2	54.8 $^{+1.7}_{-1.6}$	124.8 $^{+3.2}_{-3.1}$	143.2 $^{+3.7}_{-3.5}$	109.7 $^{+2.8}_{-2.7}$
F2	Mean	10.8 \pm 0.9	23.3 \pm 1.8	26.9 \pm 1.9	20.6 \pm 1.5	2.03 \pm 0.27	1.5 \pm 0.2	1.5 \pm 0.1	0.75 \pm 0.04	0.5(f)	142.8/139
F2	Peak1	25.7 \pm 0.9	55.5 \pm 1.8	64.1 $^{+2.0}_{-1.9}$	49.1 \pm 1.5

Note. The top section contains timing parameters for F1 and F2, and the bottom contains the joint spectral fits. (Top) The 2–8 keV fluence, mean, and peak rates each have two entries, one for observed (raw) values, the other for the pile-up corrected (corr) values. These contain both flare and quiescent counts since both contribute to pile-up during the flares. The rise time for flare F1 is measured from the flare start time to the maximum of the first peak, the decay time is measured from the maximum of the second peak to the flare stop time. For the double-peaked flare F1 each of the two peak rates are listed. (Bottom) Sgr A* flares are fit with the model $\text{fgcdust} \times \text{TBnew} \times (\text{powerlaw}_f + \text{powerlaw}_q + \text{blackbody})$, where the two power laws fit the flare and quiescent spectral components during the flare, and the blackbody fits the contribution from the magnetar. The magnetar-only fits employ a single blackbody and utilize data exclusively during Sgr A*'s quiescent periods to avoid contamination. Dust scattering and absorption are included in both fits. The quiescent PL index is fixed to $\Gamma = 3.0 \pm 0.2$ (Nowak et al. 2012; Neilsen et al. 2013). The flux contribution from the magnetar is estimated to be 3% and 2.5% for F1 (ObsID 15043) and F2 (ObsID 16218), respectively. N_H is fixed to 16.3×10^{22} cm $^{-2}$ and we assume a distance to the Galactic center of 8 kpc. Pile-up (α) is a free parameter in the F1 fit, but is fixed to $\alpha = 0.5$ for the F2 fit because it could not be constrained by the data (Section 4.3). We list the 2–8 keV absorbed and unabsorbed fluxes, as well as the 2–10 keV unabsorbed flux and luminosity. The peak flux values are derived assuming peak/mean flux ratios of 2.2 ± 0.1 , 1.9 ± 0.1 , and 2.4 ± 0.2 (90% confidence limits), for F1 peak1, F1 peak2, and the F2 peak, respectively, and errors are combined in quadrature (Section 3). Hardness ratios (HR) are defined as 4–8 keV/2–4 keV (Section 3.4).

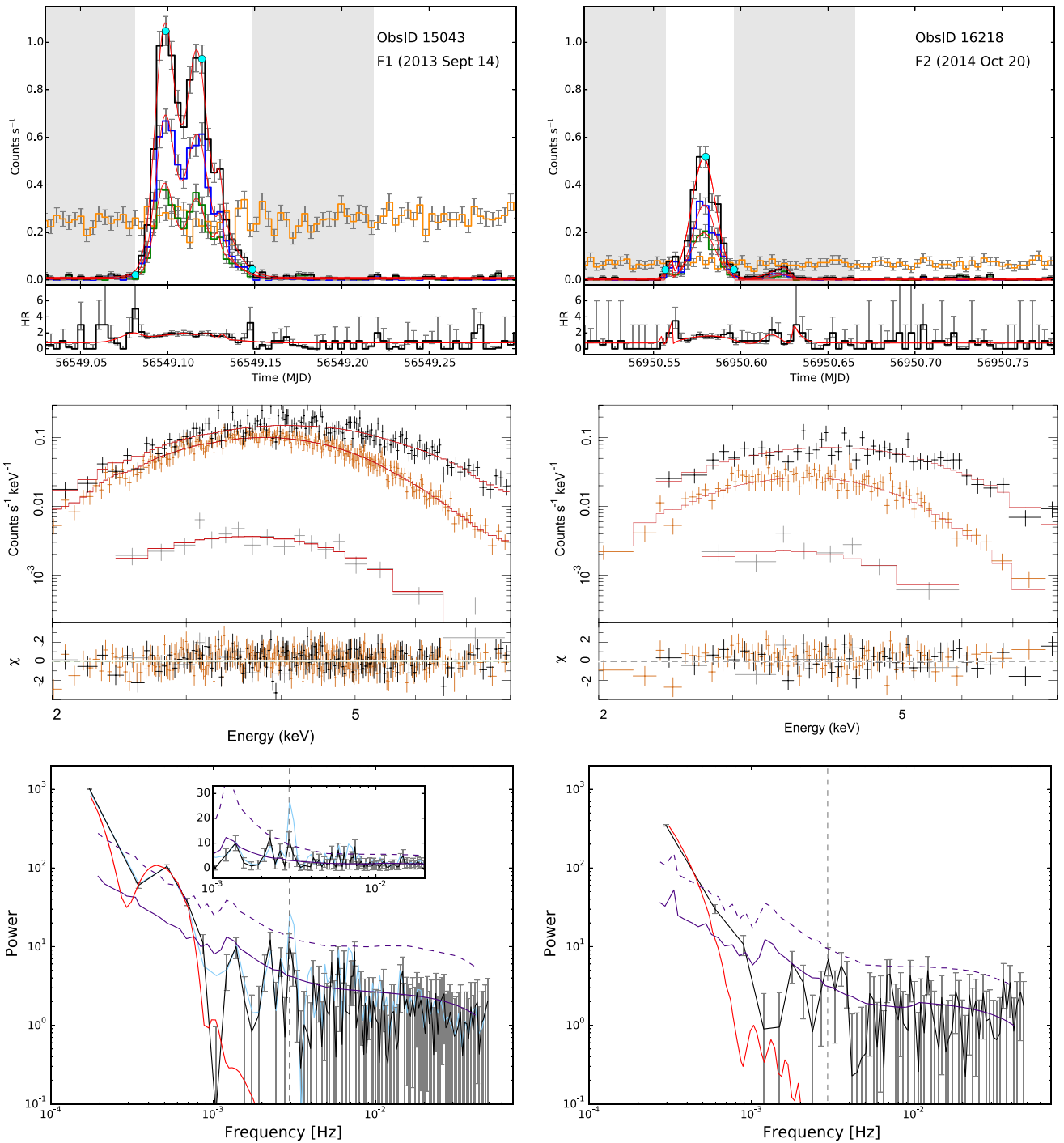


Figure 2. (Top) *Chandra* lightcurves in 300 s bins for the 2013 September 14 flare F1 in ObsID 15043 (left) and the 2014 October 20 flare F2 in ObsID 16218 (right); no pile-up correction has been applied, see instead Figure 3. The black, blue, and green curves represent emission from Sgr A* in the 2–8 keV (full), 2–4 keV (soft), and 4–8 keV (hard) bands, respectively; the orange line shows the 2–8 keV emission from the magnetar SGR J1745–2900. Smooth red lines are model fits to the Sgr A* lightcurves (Section 3.3, see also Appendix B). The flare start and stop times and brightest peaks are indicated by small cyan dots. The gray shaded areas mark times that fall outside flare and quiescent GTIs. The lower subpanels show the hardness ratio (HR = hard / soft), overplotted with the hard-to-soft model ratio from the lightcurves (solid red lines). (Middle) Pile-up-corrected X-ray spectra for F1 (left) and F2 (right). The Sgr A* flare component is in black, quiescence in gray, and the magnetar in orange, with spectral models overplotted in red (see Table 2). The lower subpanels show the χ^2 residuals for each component fit. (Bottom) Black curves are the power spectra derived via a Fast Fourier Transform for the two bright X-ray flares. The pale blue curve for F1 shows the PSD including instrumental effects and the dashed gray line marks the spurious peak in F1 at $\nu = 2.99 \pm 0.14$ mHz; this section of the PSD is also shown in the inset with the y-axis on a linear scale. We mark this frequency in the F2 PSD for reference. The dark purple solid and dashed lines mark the 50% (bottom) and 90% (top) confidence intervals for a combined red noise ($\beta = 1$) plus white noise spectrum (Section 5.1 and Appendix A)—the solid red curve shows the FFT of our fit to the 2–8 keV lightcurve (top panels).

3.4. Hardness Ratio

We calculate flare hardness ratios (HRs) as the ratio of the numbers of hard (4–8 keV) to soft (2–4 keV) photons, and plot

them in the subpanels of the lightcurves at the top of Figure 2. Errors on the hardness ratios are calculated using the Bayesian analysis described in Park et al. (2006) and are shown in the subpanels below the lightcurves in Figure 2. Bins containing

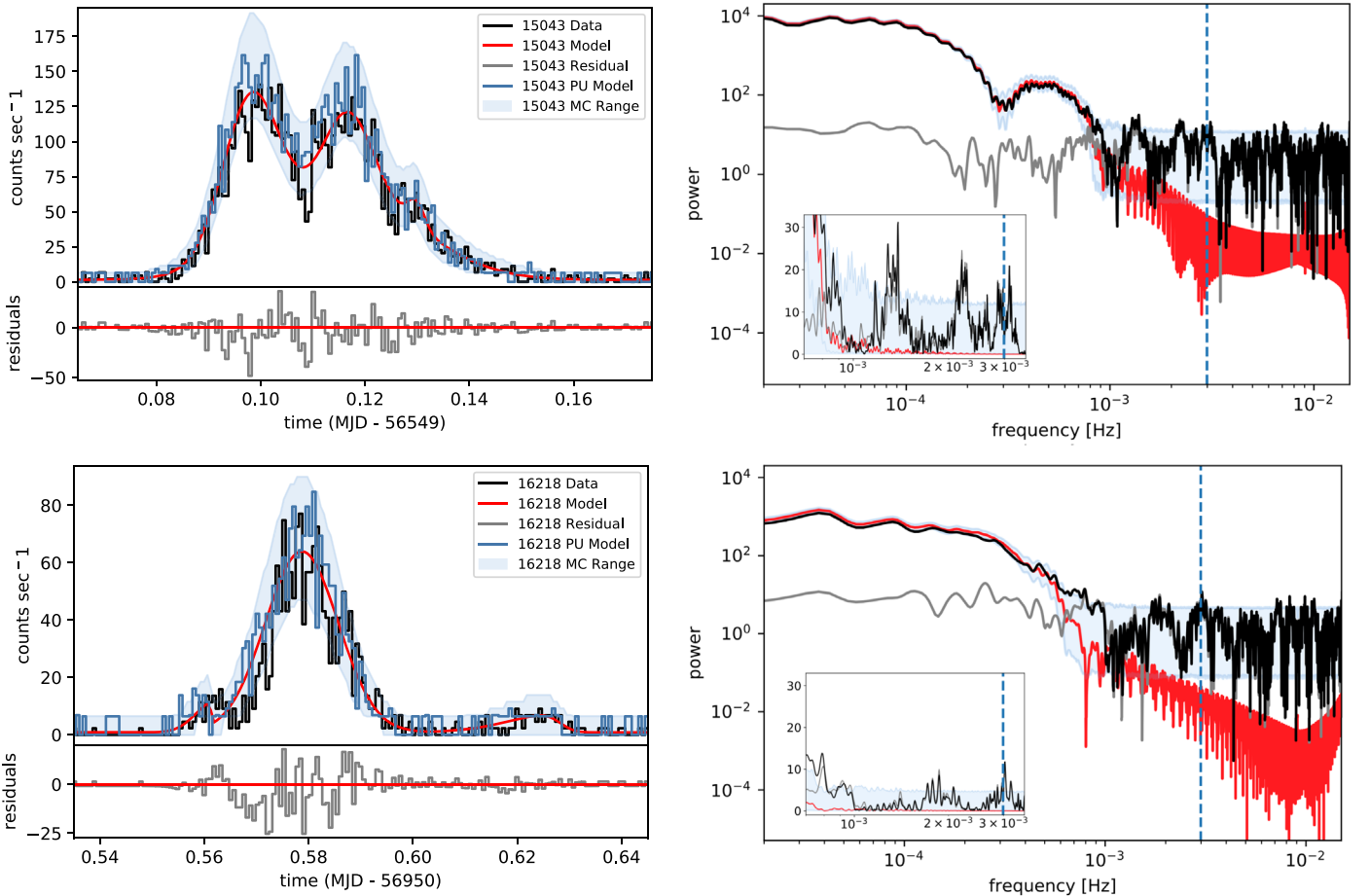


Figure 3. (Left panels) The F1 and F2 lightcurves (black line) and the best-fit model (red curve), binned to ~ 50 s (vs. the 300 s binning shown in Figure 2). The residual lightcurve (data – model) is plotted in the lower subpanel (gray line). The pile-up-corrected models are plotted as dark blue lines. Overplotted are the 5%–95% error intervals from 10,000 Monte Carlo simulations of the pile-up-corrected model, generated by adopting a randomly generated Poisson error with a value equal to the larger of either the number of counts in that frame or an expectation value based on the average quiescent count rate (Section 5.3; light blue shaded regions); binning is performed after the lightcurve simulation is complete. (Right panels) The L–S periodograms resulting from the measured and simulated lightcurves (line colors as in left-hand panel).

zero counts in the 4–8 keV lightcurve are replaced with the median quiescent count rate for plotting purposes only. The hardness ratio for F1 exhibits two peaks that coincide with the flare start/stop times. F2 has a similar structure, though it shows a more gradual increase in hardness ratio at the start of the flare, and the feature at the end of the flare is not as prominent. These features in the HR have large errors and we therefore do not consider them significant.

The HR between these two bright flares is fairly uniform, 1.7 ± 0.3 and 1.5 ± 0.2 for F1 and F2, respectively. These are consistent within errors, but somewhat lower than the average flare HR of ~ 2 for the bright X-ray flare studied by Nowak et al. (2012). Different effective areas for the ACIS-S and HETG instruments may account for this discrepancy. Pile-up also impedes our ability to measure the spectral shape and timing of the flare photons—we assess the degree of pile-up in our spectral fits in Sections 3.5 and 4.

3.5. Pile-up Correction

Pile-up occurs when two or more photons strike a pixel during a single CCD readout. The two photons are subsequently recorded as a single event with a summed energy. This information loss reduces the incident count rate and falsely hardens the spectrum for bright X-ray events like F1 and F2.

Using a 1/8 subarray for these observations lowers the frame rate to $\Delta t \sim 0.44$ s (0.4 s for the primary exposure, plus 0.04 s for readout) from a nominal $\Delta t = 3.2$ s, which mitigates the effects of pile-up, but does not fully eliminate them.

To correct the lightcurve for pile-up, we use the formula from the *Chandra* ABC Guide to Pileup,²²

$$f_r = 1 - \frac{[\exp(\alpha\Lambda) - 1][\exp(-\Lambda)]}{\alpha\Lambda} \quad (1)$$

where f_r is the fraction of the incident count rate lost due to pile-up, Λ is the incident rate, and α is the pile-up grade migration parameter. Here the rates are expressed as counts per frame rather than the standard counts per unit time. We use this parameterization to calculate a pile-up-corrected incident count rate for each ~ 50 s bin in the lightcurves shown in Figure 3. As expected, higher count rates are substantially more affected by pile-up degradation.

4. Spectral Analysis

Since Sgr A* and SGR J1745–2900 are separated by only $2''4$, we minimize spectral cross-contamination by selecting

²² http://asc.harvard.edu/ciao/download/doc/pileup_abc.ps

small extraction regions and appropriate GTIs. We perform spectral fits with the Interactive Spectral Interpretation System v1.6.2-32 (ISIS; Houck & Denicola 2000). The neutral hydrogen column absorption (N_H) is modeled with TBnew, and we use the photoionization cross sections of Verner et al. (1996) and the elemental abundances of Wilms et al. (2000). Interstellar dust can scatter X-ray photons and is a crucial component in X-ray spectral fitting of Galactic center sources (Corrales et al. 2016, 2017; Smith et al. 2016; Jin et al. 2017). We apply the dust scattering model fgcdust (Jin et al. 2017) developed for AX J1745.6–2901 and tested on X-ray sources in the Galactic center region by Ponti et al. (2017). Spectral fits are detailed in the bottom half of Table 2.

4.1. SGR J1745–2900

We extract the magnetar’s spectrum during nonflare intervals to minimize contamination from Sgr A*. The spectra from ObsID 15043 and 16218 are jointly fit using an absorbed, dust-scattered blackbody model (fgcdust*TBnew*blackbody) with the neutral hydrogen column tied between the data sets. An additional pileup component is added to the model in ObsID 15043 due to the moderately high count rate of the magnetar during this observation. The best-fit absorption column is $N_H = (16.3 \pm 0.8) \times 10^{22} \text{ cm}^{-2}$. The blackbody temperatures (kT) are allowed to vary between the observations (the magnetar is known to fade and cool on timescales of months to years), yielding values of $kT = 0.79 \pm 0.02 \text{ keV}$ and $kT = 0.75 \pm 0.04 \text{ keV}$ with 2–8 keV absorbed fluxes of $6.9 \pm 0.2 \times 10^{-12} \text{ erg s}^{-1} \text{ cm}^{-2}$ and $1.5 \pm 0.1 \times 10^{-12} \text{ erg s}^{-1} \text{ cm}^{-2}$, in agreement with Coti Zelati et al. (2015, 2017). These values for the absorption column and the magnetar temperature are adopted in the spectral fits described below.

4.2. Sgr A* Quiescence

We extract spectra of Sgr A*’s quiescent emission using the same off-flare GTIs as for SGR J1745–2900. We fit the emission with an absorbed power law model that includes dust scattering. Due to the low number of counts (~ 280 for ObsID 15043 and ~ 140 for ObsID 16218), we find that N_H and the power law index (Γ) are unconstrained when both are left free. Fixing the absorption column to the magnetar value ($N_H = 16.3 \times 10^{22} \text{ cm}^{-2}$) returns a PL index of $\Gamma_q \sim 3.7 \pm 0.5$. This value is still not well constrained, but matches quiescent spectral fits from previous studies, e.g., Nowak et al. (2012). Since Nowak et al. (2012) incorporate all available Chandra observations of Sgr A* up to 2012 (>3 Ms), which are not complicated by potential magnetar contamination, we adopt their well-constrained PL index $\Gamma_q = 3.0 \pm 0.2$ in all subsequent spectral analyses.

4.3. Sgr A* Flare

We use the on-flare GTIs to extract Sgr A* flare spectra for both observations. The majority of the photons are from the bright Sgr A* flares, but also include counts from Sgr A*’s quiescent emission, plus a small contribution from the nearby magnetar. At the position of Sgr A*, the magnetar contributes 3% and 2.5% of the flux, for F1 and F2 respectively (estimated with the ray-trace simulation ChART/MARX and approximations of the GC dust scattering halo, e.g., Corrales et al. 2017; Jin et al. 2017, and references therein). We fix the magnetar

contribution manually with the model_flux tool. We jointly fit these three components with a flare power law (powerlaw_f), a quiescent power law (powerlaw_q), and a thermal blackbody (blackbody) for the magnetar. The dust scattering model (fgcdust) and absorption (TBnew) are applied to the total spectrum.

Using the dedicated pile-up model in ISIS (see Equation (1)), we test spectral fits for F1 and F2 with and without pile-up and find that both suffer from pile-up, though we cannot directly constrain the impact for F2 ($\alpha = 0.0^{+1.0}_{-0.0}$) and instead fix it to $\alpha = 0.5$. We fix the absorption column, the quiescent photon index, and the magnetar temperatures to the values from Sections 4.1 and 4.2.

These joint spectral fits give flare power-law indices of $\Gamma = 2.06 \pm 0.14$ (F1) and $\Gamma = 2.03 \pm 0.27$ (F2), corresponding to 2–8 keV absorbed fluxes of $F_{2-8 \text{ keV}} = 28.5^{+1.7}_{-1.6} \times 10^{-12} \text{ erg s}^{-1} \text{ cm}^{-2}$ for F1 and $F_{2-8 \text{ keV}} = (10.8 \pm 0.9) \times 10^{-12} \text{ erg s}^{-1} \text{ cm}^{-2}$ for F2. We show these fits in the middle panels of Figure 2 and report the fit parameters in Table 2, together with the derived fluxes and luminosities for the flares.

As a check on our analysis, we subtract the off-flare photons from the same 1’’25 Sgr A* region using the quiescent GTI. This removes contributions from the magnetar, Sgr A*’s quiescent emission, as well as contamination from other sources in the crowded region (e.g., Sgr A East). We fit these photons with a simple absorbed power-law model fgcdust \times TBnew \times powerlaw_f, fix the absorption column, and apply a pile-up model as above. The resultant power-law indices are $\Gamma = 1.83 \pm 0.13$ and $\Gamma = 1.93 \pm 0.30$ for F1 and F2, respectively, in good agreement with our previous findings. This is a useful check on our joint spectral fits, but pileup models may not work properly on these subtracted spectra and are likely to result in harder power-law indices (Section 3.5). We thus prefer the joint spectral fits and adopt those values throughout the remainder of the text and in Table 2.

5. Power Spectra

We search for short timescale variability by creating power spectral densities (PSDs) for flares F1 and F2. We perform a fast Fourier transform (FFT) with the Leahy et al. (1983) normalization on 10 s binned lightcurves from the flare-only GTIs. The PSDs for F1 and F2 are shown in the bottom panels of Figure 2. The power spectra are complex, with broad features at lower frequencies and smaller-scale modulation at higher frequencies.

5.1. PSD Noise Analysis

We examine the broad, low-frequency features by transforming the lightcurve models described in Section 3.3 (and Appendix B) using the same FFT procedure. The resultant model PSDs are overplotted in red in the bottom panels of Figure 2. In both ObsIDs the power spectrum from the flare is well matched to the low-frequency broad curves, but with a sharp drop in power at $\sim 10^{-3} \text{ Hz}$.

We investigate the high-frequency features at $>10^{-3} \text{ Hz}$ to determine whether they can be attributed to short period variability, e.g., quasi-periodic oscillations (QPOs), versus noise in the lightcurve or aliasing, which can also produce sharp artificial features. We follow a method similar to that of Timmer & Koenig (1995; see also implementation by Mauerhan et al. 2005) and generate simulations where there

is no signal. For each flare we create 1000 data sets comprised solely of red and white noise, perform an inverse FFT, and scale the resultant lightcurves so that they have the same variance and sampling as the flare lightcurve. Since the Timmer and Koenig algorithm is prone to windowing, we generate simulated lightcurves ~ 10 times longer than our flare lightcurves. The simulated data sets are then transformed into a collection of power spectra.

Our choice of noise spectra is motivated by the detection of red noise in past observations of Sgr A* (e.g., Mauerhan et al. 2005; Meyer et al. 2008; Do et al. 2009; Witzel et al. 2012, 2018; Neilsen et al. 2015). Two values are tested for the red noise slope ($\beta = 1.0, 2.0$), which span the range of slopes detected in previous observations (Yusef-Zadeh et al. 2006; Meyer et al. 2008) and simulations (Dolence et al. 2012). At higher frequencies the flare PSD curves taper off into flat Poisson noise, and we therefore also include white noise ($P(f) \sim f^0 = 1$) in our simulations for a total noise model of $P(f) = f^{-\beta} + 1$. The simulated PSD curves for two choices of β are shown in Appendix A; for clarity only the results for $\beta = 1.0$ are plotted in the bottom panels of Figure 2, where the 50% and 90% confidence intervals are shown as purple solid and dashed lines, respectively.

F1 has three features that rise above the 90% confidence interval: two broad curves at lower frequencies and a sharp peak at $\nu \sim 3$ mHz (pale blue curve, most prominent in the inset in the bottom left panel of Figure 2). The first two broad features at $\nu \sim 0.17$ mHz (5.7 ks) and $\nu = 0.49$ mHz (2.0 ks) arise from the large-scale features in the lightcurve captured by our model, but we cannot attribute the third, narrower peak to the gross morphology of the flare, as it is located well after the flare envelope model drops in power. We fit this peak with a Lorentzian centered at $\nu = 2.99 \pm 0.01$ mHz, with a width of $\delta\nu = 0.26 \pm 0.04$ mHz, and a quality factor of $q = \nu/\delta\nu = 11.3$. We indicate this frequency on the PSDs as a vertical dashed line in the bottom panels of Figure 2, but argue in Section 5.2 that it is an instrumental artifact. The residual lightcurves and PSDs in Figure 3 (dark gray lines) show the result of subtracting this large-scale component and indicate the remaining unmodeled structure. Hence, removing the flare envelop (fitted in the time domain) before searching for high frequency features introduces a spurious signal in the PSD and we do not pursue this approach further here. The only portion of the F2 PSD that rises above the 90% confidence interval is the flare envelope at low frequencies, there are no significant high-frequency features. We mark the 2.99 mHz position in the F2 PSD for comparison only.

5.2. Bad Pixel Analysis

The *Chandra* spacecraft dithers its pointing position to reduce the effects of bad pixels, nodal boundaries, and chip gaps during an observation, as well as to average the quantum efficiency of the detector pixels.²³ This observational requirement can introduce spurious timing signatures at either the pitch (X) or yaw (Y) dither periods or their harmonics.

For ObsID 15043 we create an image binned in chip coordinates and extract photons from the same $1''25$ region centered on Sgr A* from the level 1 and level 2 event files. Both show the standard Lissajous dither pattern, but also two pixel columns that have been flagged as bad and thus excised in

the standard level 2 files. As the Sgr A* extraction region crosses this sharp nodal boundary, the masked pixels create a discontinuity in the lightcurve that manifests as a peak in the power spectrum of F1, at half the period of the yaw dither (because Sgr A* crosses the column of bad pixels twice per oscillation). The Sgr A* extraction region in ObsID 16218 does not overlap a bad column, and SGR J1745–2900 is similarly unaffected in both ObsIDs. Analyses of the Sgr A* and SGR J1745–2900 lightcurves extracted from ObsID 16218 do not reveal any flagged pixels.

In light of this finding, we create new lightcurves for F1 in ObsID 15043 without removing the bad pixel columns, and use these for all subsequent timing analysis. We adopt the extraction region, lightcurve binning, and GTI filtering described in Section 3. The resultant power spectrum is shown in black in the bottom left panel of Figure 2, while the pale blue curve represents the standard level 2 *Chandra* filtering with the flagged columns removed. The peak at ~ 3 mHz is no longer detected and we conclude that the possible QPO in F1 arises from instrumentation effects and cannot be attributed to Sgr A*.

5.3. PSD Permutation Error Analysis

To investigate the high frequency features still apparent in the PSDs, we perform a Monte Carlo (MC) permutation to simulate the errors on the X-ray lightcurves and PSDs. We create 10,000 MC simulations of the full, unbinned *Chandra* lightcurve (rather than the flare-only intervals) by drawing a simulated count rate for each *Chandra* frame (frame time = 0.44 s for a 1/8 subarray), using our model for the counts from Section 3.3 and Appendix B and a randomly generated Poisson error with an expectation value equal to the larger of (1) the number of counts in that frame or (2) a constant expectation value (the expected number of counts) equal to the average quiescent count rate times the frame time, i.e., 0.004 and 0.003 for ObsID 15043 and 16218. This expectation value is critical for frames where zero counts are detected.

We generate a Lomb–Scargle (L–S; Scargle 1982) periodogram for each simulated model lightcurve, which is subsequently binned (125 frames are combined to create ~ 50 s bins) and corrected for pile-up. The left upper panels of Figure 3 show the measured lightcurves (black lines), unbinned model fits (smooth red lines), and binned, pile-up-corrected models (dark blue lines), as well as the 5%–95% confidence intervals from the MC simulations (light blue shaded regions). The lower subpanels on the left show the residual between the data and the model (gray lines). The right-hand panels show the resultant LS periodogram on a log scale for each of these components and the insets highlight a subset of the higher frequencies. The black curves from the measured LS periodograms have small peaks that rise just above the 95% c.l., but these are weak and most likely attributable to instrumental effects, noise, harmonics of the power in the stronger flare envelopes, and/or aliasing (see Appendix A).

6. Discussion

Our analysis reveals two of the brightest X-ray flares seen so far from Sgr A*, with peak 2–10 keV luminosities of 12.3×10^{35} erg s⁻¹ (F1) and 49.1×10^{34} erg s⁻¹ (F2), durations of 5.7 and 3.4 ks, and total energies $(0.7\text{--}3.3) \times 10^{39}$ erg. These

²³ <http://cxc.harvard.edu/proposer/POG/html/chap5.html#tb:dither>

are as large or larger than the peak luminosities, durations, and energies found for previously detected bright X-ray flares from *Chandra* ($L_{2-10\text{ keV}} = 48 \times 10^{34} \text{ erg s}^{-1}$, 5.6 ks, $E_{2-10\text{ keV}} \sim 10^{39} \text{ erg}$; Nowak et al. 2012) and *XMM-Newton* ($L_{2-10\text{ keV}} \sim (12-19) \times 10^{34} \text{ erg s}^{-1}$, (2.8–2.9) ks, $E_{2-10\text{ keV}} = (0.3-0.5) \times 10^{39} \text{ erg}$; Porquet et al. 2008; Nowak et al. 2012).

6.1. Flare Emission Scenarios

The X-ray spectral indices for F1 and F2 are consistent with $\Gamma \sim 2$, similar to other bright X-ray flares but significantly harder than the spectrum in quiescence ($\Gamma \sim 3$; Nowak et al. 2012). Together with constraints from the NIR, the spectrum seems to favor a synchrotron emission scenario wherein the NIR and X-ray spectral indices are set by the particle acceleration process (Markoff et al. 2001; Dodds-Eden et al. 2009). When the NIR is bright, the spectral index is well described by $\nu f_\nu \propto \nu^{0.5}$ (e.g., Hornstein et al. 2007; Ponti et al. 2017) and synchrotron models predict a cooling break, such that $\Gamma \sim 2$ at X-ray wavelengths. Evidence of a similar spectral index for bright and faint flares (e.g., Neilsen et al. 2013) also supports this interpretation.

Alternative models invoke Compton processes (e.g., Markoff et al. 2001; Eckart et al. 2008; Yusef-Zadeh et al. 2012). However, because the Compton bump can shift due to changing scattering optical depths or electron energies (or other factors) flare spectra should show a range of spectral indices. Hence there is no clear expectation that a constant NIR spectral index will lead to a constant X-ray photon index. On the other hand, the large difference between NIR and X-ray cumulative distribution functions (Witzel et al. 2012, 2018; Neilsen et al. 2015) is not easily understood within the synchrotron scenario (Dibi et al. 2016). We must continue to build up the statistics of simultaneous IR and X-ray flares to distinguish between these models.

In addition to their spectral properties, X-ray studies of Sgr A* point to a characteristic timescale for bright flares of $\sim 3-6$ ks (detectable at all durations, e.g., Porquet et al. 2003, 2008; Neilsen et al. 2013). This timescale is also consistent with F1 and F2, reported here. If we associate this timescale with a Keplerian orbital period then the orbital radius is 0.3–0.5 au, roughly two times the radius of the innermost stable circular orbit (ISCO) for a stationary black hole with Sgr A*’s mass and distance (Boehle et al. 2016; Gravity Collaboration et al. 2018b). This is equivalent to $\sim 5 \times$ the Schwarzschild radius (R_S ; see detailed models in Markoff et al. 2001; Liu & Melia 2002; Liu et al. 2004; Dodds-Eden et al. 2011). In this scenario, the flare emission is likely to arise from structures very near or at the event horizon.

Alternatively, we can estimate the size of the emission region (the emitting “spot”) by comparing the total X-ray energy radiated by the brightest flare, $E_{2-10\text{ keV}} = 3.3 \times 10^{39} \text{ erg}$, to the energy available in the accretion flow. The volume of the accretion flow that contains an equal amount of magnetic energy is approximately $E_B = (B^2/8\pi)(4\pi R_{\text{spot}}^3)$. Setting this equal to the flare’s total energy radiated in X-rays ($E_{2-10\text{ keV}}$) and assuming $B = B_0 (R_f/3R_S)^{-1}$, where $B_0 = 30 \text{ G}$ is the magnetic field strength scaled to a typical value close to the black hole (Yuan et al. 2003; Dodds-Eden et al. 2009; Mościbrodzka et al. 2009; Dexter et al. 2010; Ponti et al. 2017), and R_f is the flare

emission radius, gives

$$R_{\text{spot}} \sim 2 \left(\frac{R_f}{3R_S} \right)^{2/3} \left(\frac{B_0}{30 \text{ G}} \right)^{-2/3} \left(\frac{E_{2-10\text{ keV}}}{3.3 \times 10^{39} \text{ erg}} \right)^{1/3} R_S. \quad (2)$$

Powering this flare requires a relatively large emitting volume, even assuming a 100% efficiency of converting magnetic energy into X-rays. Increasing the flare emission radius makes the relative size of the hot spot smaller, but only slowly. This poses challenges for explaining the rapid changes in the luminosity (e.g., this work, Barrière et al. 2014, among others), though an increase in the strength of the magnetic field in the flare region could allow a smaller volume. In general, this represents a lower limit on the size of the flare’s total emitting region, because it only takes X-rays into account. It is also consistent with a scenario in which the size of the emitting region is larger for brighter flares.

Recent results from the GRAVITY experiment on the Very Large Telescope Interferometer (VLTI, Gravity Collaboration et al. 2018b), argue that Sgr A*’s infrared variability can be traced to orbital motions of gas clouds with a period of ~ 45 minutes (2.7 ks). Using ray-tracing simulations, they match this timescale to emission from a rotating, synchrotron-emitting “hot spot” in a low inclination orbit at $\sim 3-5 R_S$ (Gravity Collaboration et al. 2018a).

Since near-IR and X-ray outbursts from Sgr A* appear to be nearly simultaneous and highly correlated (e.g., Boyce et al. 2019), these well-matched timescales give further support to hot spot models and to emission scenarios where the NIR and X-ray emission originates near the SMBH’s event horizon. We caution, however, that this timescale is not unique, and can also be reproduced by the tidal disruption of asteroid-size objects (Čadež et al. 2008; Kostić et al. 2009; Zubovas et al. 2012) and the Alfvén crossing time for magnetic loops near the black hole (Yuan et al. 2003; Yuan & Narayan 2004).

The GRAVITY NIR flare detected on 2018 July 28 is also double-peaked (see Figure 2 of Gravity Collaboration et al. 2018a), much like F1 reported in this work. The durations of these two outbursts, ~ 115 minutes for the NIR and ~ 97 minutes for the X-ray, are similar and the time between the two peaks, ~ 40 minutes (NIR) and ~ 30 minutes (X-ray), are also similar. The ratio of the total flare duration to the time between peaks is approximately a factor of 3 in both cases. Double-peaked flares like these have previously been detected from Sgr A* (e.g., Mossoux et al. 2015; Karssen et al. 2017; Fazio et al. 2018; Boyce et al. 2019), but even when they do not have multiple peaks, bright X-ray flares often display asymmetric lightcurve profiles (e.g., this work, Porquet et al. 2003, 2008; Nowak et al. 2012; Mossoux et al. 2016). Further investigation of their statistical and timing properties is ripe for further study.

Despite differences in their morphologies, other flare properties follow more predictable trends. Neilsen et al. (2013) present relationships between the fluence, count rate, and duration of ~ 40 flares from the XVP. To compare F1 and F2 to the XVP flare population, we adjust for the different instrument configurations using PIMMS²⁴ and scale the reported XVP flare fluences to their equivalent ACIS-S values (Figure 4). F1 and F2 (filled dark blue circles) are considerably brighter than most of the XVP sample, but show the same trend toward higher fluences at longer durations. This again supports a scenario in which the emission region is larger for brighter

²⁴ *Chandra* proposal tools: <http://cxc.harvard.edu/toolkit/pimms.jsp>.

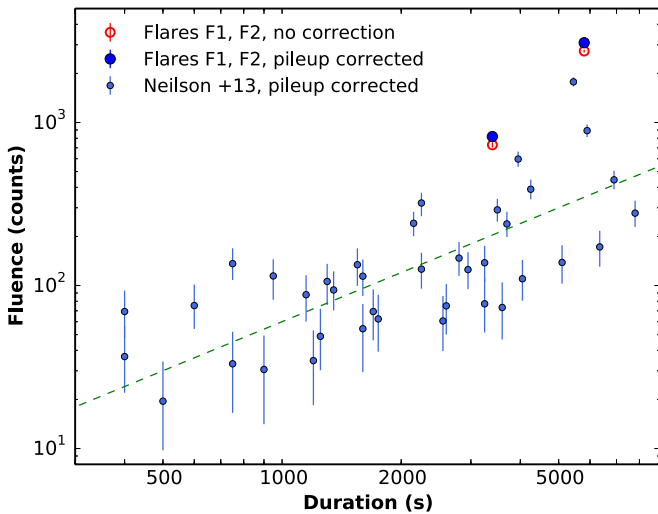


Figure 4. The 2–8 keV flare fluence as a function of flare duration. The large blue and red data points represent the incident and pile-up corrected data, respectively, for F1 and F2. Smaller blue points represent the flares reported in Neilsen et al. (2013). Originally reported as fluxes from the HETG configuration, the values were converted to ACIS-S counts for a uniform comparison with the data presented in this work. The dashed green line, from Neilsen et al. (2013), represents flares with luminosities $L = 5.4 \times 10^{34}$ ergs s^{-1} , the approximate demarcation between “bright” flares and “dim” flares.

flares. However, our observations and detection techniques are biased against long-duration, low fluence (i.e., low contrast) flares. Comprehensive flare simulations are under development (e.g., Bouffard et al. 2019) and will aide in diagnosing these and other observational biases.

The flare X-ray hardness ratios and spectral indices appear to be constant, indicating that the spectral slope does not change significantly over the duration of the flare. Strengthening this argument, the three brightest X-ray flares detected before our discoveries have photon spectral indices of $\Gamma = 2.0_{-0.6}^{+0.7}$, 2.3 ± 0.3 , and $2.4_{-0.3}^{+0.4}$ (Porquet et al. 2003, 2008; Nowak et al. 2012), which are similar to our results of $\Gamma = 2.06 \pm 0.14$ and 2.03 ± 0.27 for F1 and F2. Recent results from *NuSTAR* at higher energies (3–79 keV) provide additional support for a constant PL slope—Zhang et al. (2017) report photon indices of $\Gamma \sim 2.0$ – 2.8 ± 0.5 (90% confidence) for seven Sgr A* flares. Hence, it appears that Sgr A*’s bright X-ray flares belong to the same population (Section 3.4), and thus are likely to arise from the same energy injection mechanism.

6.2. Multiwavelength Coverage

Multiwavelength campaigns targeting Sgr A* often emphasize variability in the X-ray and infrared (e.g., recent studies by Fazio et al. 2018; Boyce et al. 2019; and references therein), where emission peaks are nearly simultaneous. Unfortunately, neither F1 nor F2 have near-IR coverage. The GRAVITY Collaboration has demonstrated the power of NIR interferometry in resolving structures only ~ 10 times the gravitational radius of Sgr A* and future simultaneous observations with this instrument and *Chandra* could offer a powerful probe of how bright X-ray flares are linked to changes in the accretion dynamics near the event horizon.

Longer wavelength observations have hinted at a lag between X-ray flares and their candidate submillimeter or radio counterparts, with the long wavelength data lagging the

X-ray. Capellupo et al. (2017) report nine contemporaneous X-ray and Jansky Very Large Array (JVLA) radio observations of Sgr A*, including coverage of the F1 flare. The JVLA lightcurve overlapping F1 lasts ~ 7 hr and shows significant radio variability at 8–10 GHz (X-band) in the form of a 15% (0.15 Jy) increase during the second half of the observation. The radio lightcurve is not long enough to show a clear start or stop time for the rise, but Capellupo et al. (2017) determine a lower limit on the radio flare duration of ~ 176 minutes, compared to ~ 100 minutes for the full X-ray flare, with the radio rising before and peaking after the X-ray. This delay could be understood in the context of the adiabatic expansion of an initially optically thick blob of synchrotron-emitting relativistic particles (e.g., Yusef-Zadeh et al. 2006), offering an alternative to the hot spot models discussed above. However, due to the incomplete temporal coverage for F1 and inconclusive correlations between the other radio and X-ray peaks in the study, Capellupo et al. (2017) suggest that stronger X-ray flares may lead to longer time lags in the radio, but do not find strong statistical evidence that the radio and X-ray are correlated.

Observations at 1 mm were also performed at the Submillimeter Array (SMA) a few hours in advance of the F1 flare and on subsequent days as part of a long-term monitoring program (Bower et al. 2015). These observations show flux densities that are significantly above the historical average on the date of the F1 flare and for approximately one week afterwards. It is difficult to associate these high flux densities directly with the F1 flare, however, given the infrequent sampling of the SMA lightcurves and the characteristic timescales of millimeter/submillimeter variability (approximately 8 hr, Dexter et al. 2014).

The lack of infrared and patchwork of longer wavelength observations for F1 (and the paucity of multiwavelength data for F2), underscores the importance of continued multi-wavelength monitoring of Sgr A*.

Toward this end, the *Event Horizon Telescope* (EHT; Doeleman et al. 2008) has recently undertaken its first full-array observations of Sgr A* and M87*. These have offered exquisite, high-precision submillimeter imaging of M87*’s event horizon (Event Horizon Telescope Collaboration et al. 2019a) and are poised to do the same for Sgr A*. Coordinated EHT and multiwavelength observations, including with approved *Chandra* programs, have begun to inform models for M87* (Event Horizon Telescope Collaboration et al. 2019b) and will soon enable a detailed comparison between Sgr A*’s X-ray and submillimeter emission, offering a new understanding of its flares and underlying accretion flow.

7. Conclusion

We have performed an extensive study of the two brightest *Chandra* X-ray flares yet detected from Sgr A*, discovered on 2013 September 14 (F1) and 2014 October 20 (F2). After correcting for contamination from the nearby magnetar, SGR J1745–2900, and observational and instrumental effects from the Galactic center X-ray background, pile-up, and telescope dither, we report the following key findings:

1. The brightest flare F1 has a distinctive double-peaked morphology, with individual peak X-ray luminosities more than $600\times$ and $550\times$ Sgr A*’s quiescent luminosity. The

second bright flare F2 also has an asymmetric morphology and rises $245\times$ above quiescence.

2. These bright flares have long durations, 5.7 ks (F1) and 3.4 ks (F2), and rapid rise and decay times: F1 rises in 1500 s and decays in 2500 s, while F2 rises in 1700 s and decays in 1400 s. These timescales may correspond to emission from a hot spot orbiting the SMBH, in agreement with new NIR results from the GRAVITY experiment. Their timing properties also imply that the size of the emitting region may scale with the brightness of the flare.
3. Both flares have X-ray spectral indices and hardness ratios significantly harder than during quiescence, $\Gamma = 2.06 \pm 0.14$ and $\Gamma = 2.03 \pm 0.27$ versus $\Gamma = 3.0 \pm 0.2$ in quiescence, consistent with previously detected Sgr A* flares and with a synchrotron emission mechanism, though Compton emission models are not ruled out.
4. Statistical tests of the flare time series, including Monte Carlo simulations of their noise properties, offer little evidence for high-frequency power (e.g., QPOs) in either flare.
5. F1 and F2 are the brightest X-ray flares ever detected by *Chandra*, and are among the brightest X-ray flares from Sgr A* detected by any observatory. They appear to deviate in the fluence-duration plane from the distribution of fainter flares detected in the 2011 Sgr A* *Chandra* XVP. However, low fluence, long duration flares may not exist or may suffer from selection bias, making this finding tentative at present.
6. Neither F1 nor F2 have near-IR coverage, but some (near-) simultaneous coverage of F1 was collected at radio and submillimeter wavelengths. These data point to higher than average flux levels for Sgr A* near the F1 outburst, but do not allow definitive correlation between Sgr A*'s X-ray and longer wavelength behavior. Coordinated multiwavelength campaigns thus continue to be essential for a complete, statistically robust examination of Sgr A*'s multiwavelength variability.

The authors thank Charles Gammie, Tiffany Kha, Matthew Stubbs, and Nicolas Cowan for discussions related to this work. We acknowledge the *Chandra* scheduling, data processing, and archive teams for making these observations possible. This work was supported by *Chandra* Award Numbers GO3-14121A and GO4-15091C, issued by the *Chandra X-ray Observatory Center*, which is operated by the Smithsonian Astrophysical Observatory for and on behalf of the National Aeronautics Space Administration (NASA) under contract NAS8-03060.

D.H., M.N., and C.O.H. acknowledge support from the Natural Sciences and Engineering Research Council of Canada (NSERC) Discovery Grant. D.H. and M.N. also thank the Fonds de recherche du Québec–Nature et Technologies (FRQNT) Nouveaux Chercheurs program. D.H. acknowledges support from the Canadian Institute for Advanced Research (CIFAR). M.N. acknowledges funding from the McGill Trottier Chair in Astrophysics and Cosmology. G.P. acknowledges financial support from the Bundesministerium für Wirtschaft und Technologie/Deutsches Zentrum für Luft- und Raumfahrt (BMWi/DLR, FKZ 50 OR 1812, OR 1715 and OR 1604) and the Max Planck Society. S.M. is funded by a VICI

grant (639.043.512) from the Netherlands Organisation for Scientific Research.

Facility: CXO.

Software: Python, CIAO.

Appendix A Power Spectra Comparisons

In addition to the power spectral analysis of the two bright Sgr A* flares presented in Section 5, we further investigate Sgr A* during quiescence to compare the respective behaviors at high frequencies. We obtain the quiescent PSD from the GTIs listed in Table 1 and process it with the same method as for the flare (see Section 5). For an additional comparison, we also obtain the power spectrum for the magnetar SGR J1745–2900 during the intervals when Sgr A* is in quiescence to minimize contamination. The resultant Leahy-normalized PSDs are shown in Figure 5 for ObsID 15043 (left) and ObsID 16218 (right). The Sgr A* flare and quiescence PSDs are plotted in black and blue, respectively, and the magnetar PSD is shown in orange.

F1 and F2 exhibit broad features at $f < 10^{-3}$ Hz attributed to the flare envelopes as discussed in Section 5 and shown in Figure 2. In contrast, at higher frequencies ($f > 10^{-2}$ Hz) both flares drop in power such that the flare PSDs overlap with or are within the uncertainties of the Sgr A* quiescent and magnetar data. Behavior in this regime is thus not unique to the flares, and can be attributed to noise. Within the frequency range ($10^{-3} < f < 10^{-2}$ Hz), however, the flare PSDs show hints of several small peaks that are not as visible in the quiescent or magnetar power spectra. These small-scale features have low significance and may be due to the instrumental effects discussed in Section 5.2 or harmonics of the structure from the flare envelope. Note that the ~ 3 s ($\sim 3 \times 10^{-1}$ Hz) period of the magnetar would not be visible on the frequency range plotted in Figure 5.

We probe these midfrequency features by exploring two independent methods of quantifying the significance of the PSD, discussed in detail in Sections 5.1 and 5.3. For the latter, we perform Monte Carlo simulations of the flare lightcurve, and for the former we generate PSDs under the worst-case assumption that all the flare photons arise from a combination of red and white noise. Figure 2 shows the 50% and 90% confidence intervals where the red noise is defined by a slope of $\beta = 1.0$. The spurious ~ 3 mHz QPO is the only feature aside from the flare envelope that rises above the noise curve.

However, a range of red noise slopes are possible in Sgr A* (see Section 5.1) and we therefore investigate the significance of the power spectral features where $\beta = 2.0$ represents the red noise. Figure 6 shows the PSD for the flare F1 with the standard *Chandra* data processing in pale blue and the updated filtering defined in Section 5.2 in black. While the two curves are very similar, the QPO resulting from instrumentation effects is clearly seen in the blue PSD. Overlaid are the error curves from the simulations where the red noise is defined with slopes of $\beta = 1.0$ and $\beta = 2.0$ in dark purple and dark yellow, respectively. The 50% confidence intervals are represented by a solid line, while the 90% confidence limits (c.l.) are dashed.

The white noise $\beta = 0$ is dominant at higher frequencies, while the red noise component is relevant in the lower

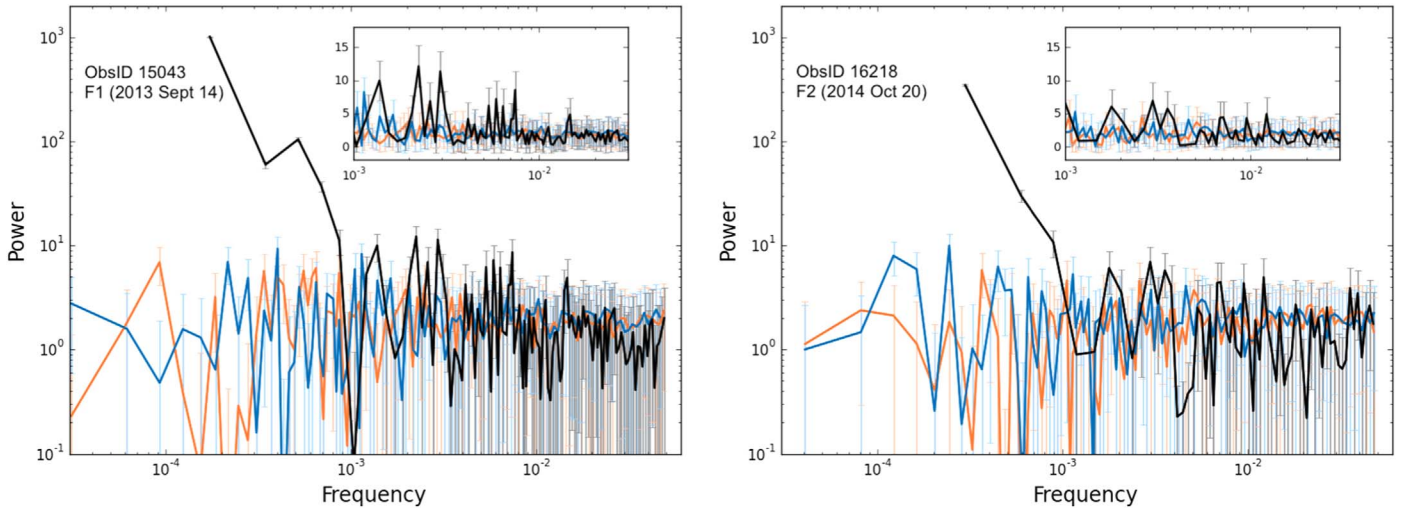


Figure 5. Leahy-normalized power spectra for Sgr A* flares F1 and F2 (black), Sgr A* during quiescence (blue), and the magnetar, SGR J1745–2900 (orange). PSDs are shown for ObsID 15043 (left) and 16218 (right).

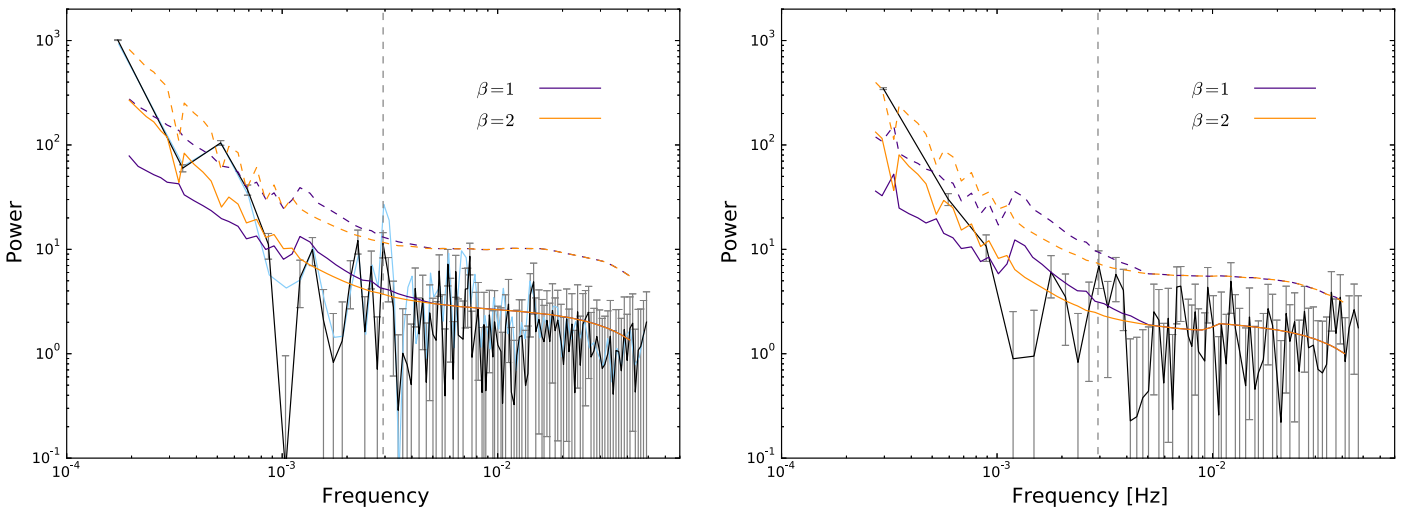


Figure 6. Leahy-normalized power spectral densities, derived via a fast Fourier transform (FFT), for the bright flare F1 (left) and flare F2 (right). The pale blue curve for F1 shows the PSD from data obtained with standard *Chandra* data processing, which includes instrumental effects. The spurious QPO at $\nu = 2.99$ mHz in flare F1 is indicated by the dashed gray line, it is shown for flare F2 on the right for comparison only. The black curve shows the PSD with proper data filtering (Section 5.2). For both flares, errors with $\beta = 1.0$ and $\beta = 2.0$ are shown in dark purple and dark yellow, respectively. The solid lines indicate 50% contours, while the dashed represent 90% contours.

frequency regime. This is evident as the curves with $\beta = 1.0$ and $\beta = 2.0$ diverge at $f < 10^{-3}$ Hz. In both scenarios there are a few features that rise above the solid 50% c.l., but none that rise above the dashed 90% confidence intervals and we conclude that no high frequency signal is detected in these bright flares.

Appendix B Lightcurve Models

The models fit to the X-ray lightcurves for F1 and F2, and used in the analyses above, are composed of a sum of four Gaussians plus a constant for F1, and a sum of two Gaussians and two skewed Gaussians plus a constant for F2. These take

the standard functional forms

$$g(t; A, \mu, \sigma) = \frac{A}{\sigma\sqrt{2\pi}} e^{-(t-\mu)^2/2\sigma^2} \quad (3)$$

$$f(t; A, \mu, \sigma, \gamma) = \frac{A}{\sigma\sqrt{2\pi}} e^{-(t-\mu)^2/2\sigma^2} \left\{ 1 + \operatorname{erf} \left[\frac{\gamma(t-\mu)}{\sigma\sqrt{2}} \right] \right\} \quad (4)$$

where the parameters are amplitude (A), center (μ), characteristic width (σ), and gamma (γ), and $\operatorname{erf}()$ is the error function.

We plot these components in Figure 7 and give the detailed fits in Table 3 for reference. The composite lightcurve models for F1 and F2 are shown as solid red lines in the top panels of Figure 2 and in all four panels of Figure 3.

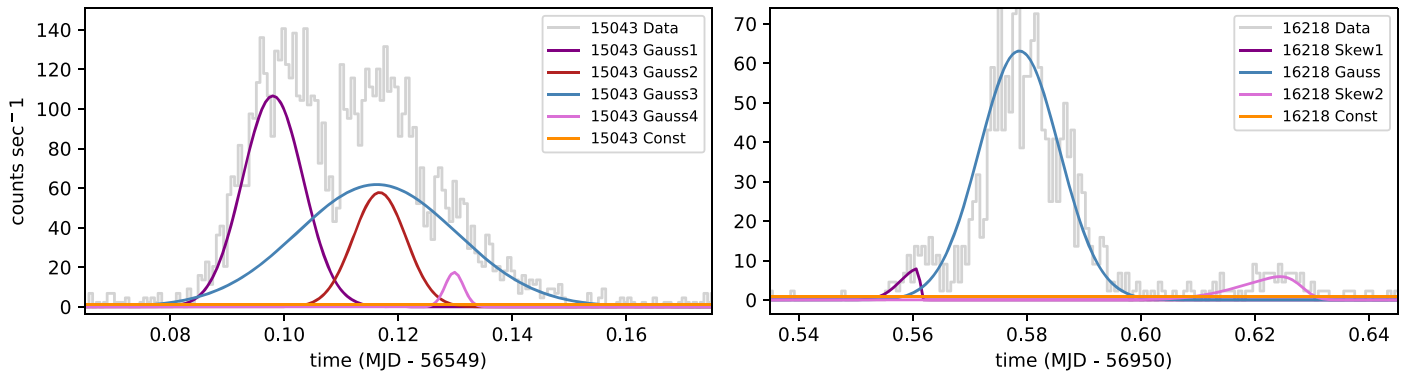


Figure 7. Model components for the F1 and F2 lightcurve fits from Equations (3) and (4) and parameters in Table 3. The composite models are plotted as red curves in the top panels of Figure 2 and in all four panels of Figure 3. The *Chandra* X-ray data are shown in light gray, with ~ 100 s binning (see Section 5.3).

Table 3
Lightcurve Models

Function	A (cnts/s)	μ (MJD)	σ (MJD)	γ
15043				
Gaussian 1	0.0114	56549.098	0.0053	...
Gaussian 2	0.0173	56549.116	0.0140	...
Gaussian 3	0.0054	56549.117	0.0046	...
Gaussian 4	0.0006	56549.130	0.0016	...
Constant	0.0112
16218				
Skew Gauss 1	0.0003	56950.561	0.0034	-15.950
Gaussian	0.0089	56950.579	0.0070	...
Skew Gauss 2	0.0006	56950.628	0.0094	-4.278
Constant	0.0066

Note. The lightcurve models for F1 and F2 are described by the parameters above, using a combination of Equations (3) and (4). Each component is shown separately in Figure 7 and the composite models are plotted as red curves in the top panels of Figure 2 and in all four panels of Figure 3.

ORCID iDs

Daryl Haggard <https://orcid.org/0000-0001-6803-2138>
 Melania Nynka <https://orcid.org/0000-0002-3310-1946>
 Michael Nowak <https://orcid.org/0000-0001-6923-1315>
 Craig Heinke <https://orcid.org/0000-0003-3944-6109>
 Joseph Neilsen <https://orcid.org/0000-0002-8247-786X>
 Jason Dexter <https://orcid.org/0000-0003-3903-0373>
 P. Chris Fragile <https://orcid.org/0000-0002-5786-186X>
 Geoffrey C. Bower <https://orcid.org/0000-0003-4056-9982>
 Lia R. Corrales <https://orcid.org/0000-0002-5466-3817>
 Nathalie Degenaar <https://orcid.org/0000-0002-0092-3548>
 Sera Markoff <https://orcid.org/0000-0001-9564-0876>
 Mark R. Morris <https://orcid.org/0000-0002-6753-2066>
 Gabriele Ponti <https://orcid.org/0000-0003-0293-3608>
 Nanda Rea <https://orcid.org/0000-0003-2177-6388>
 Jörn Wilms <https://orcid.org/0000-0003-2065-5410>

References

- Baganoff, F. K., Bautz, M. W., Brandt, W. N., et al. 2001, *Natur*, 413, 45
 Baganoff, F. K., Maeda, Y., Morris, M., et al. 2003, *ApJ*, 591, 891
 Ball, D., Özel, F., Psaltis, D., & Chan, C.-K. 2016, *ApJ*, 826, 77
 Ball, D., Özel, F., Psaltis, D., Chan, C.-K., & Sironi, L. 2018, *ApJ*, 853, 184
 Barrière, N. M., Tomsick, J. A., Baganoff, F. K., et al. 2014, *ApJ*, 786, 46
 Bélanger, G., Goldwurm, A., Melia, F., et al. 2005, *ApJ*, 635, 1095
 Boehle, A., Ghez, A. M., Schödel, R., et al. 2016, *ApJ*, 830, 17
 Bouffard, É., Haggard, D., Nowak, M. A., et al. 2019, *ApJ*, 884, 148
 Bower, G. C., Markoff, S., Dexter, J., et al. 2015, *ApJ*, 802, 69
 Boyce, H., Haggard, D., Witzel, G., et al. 2019, *ApJ*, 871, 161
 Čadež, A., Calvani, M., & Kostić, U. 2008, *A&A*, 487, 527
 Capellupo, D. M., Haggard, D., Choux, N., et al. 2017, *ApJ*, 845, 35
 Corrales, L. R., García, J., Wilms, J., & Baganoff, F. 2016, *MNRAS*, 458, 1345
 Corrales, L. R., Mon, B., Haggard, D., et al. 2017, *ApJ*, 839, 76
 Coti Zelati, F., Rea, N., Papitto, A., et al. 2015, *MNRAS*, 449, 2685
 Coti Zelati, F., Rea, N., Papitto, A., et al. 2017, *MNRAS*, 471, 1819
 Cuadra, J., Nayakshin, S., & Martins, F. 2008, *MNRAS*, 383, 458
 Cuadra, J., Nayakshin, S., Springel, V., & Di Matteo, T. 2005, *MNRAS*, 360, L55
 Cuadra, J., Nayakshin, S., Springel, V., & Di Matteo, T. 2006, *MNRAS*, 366, 358
 Degenaar, N., Miller, J. M., Kennea, J., et al. 2013, *ApJ*, 769, 155
 Dexter, J., Agol, E., Fragile, P. C., & McKinney, J. C. 2010, *ApJ*, 717, 1092
 Dexter, J., Kelly, B., Bower, G. C., et al. 2014, *MNRAS*, 442, 2797
 Dibi, S., Markoff, S., Belmont, R., et al. 2014, *MNRAS*, 441, 1005
 Dibi, S., Markoff, S., Belmont, R., et al. 2016, *MNRAS*, 461, 552
 Do, T., Ghez, A. M., Morris, M. R., et al. 2009, *ApJ*, 691, 1021
 Do, T., Hees, A., Ghez, A., et al. 2019, arXiv:1907.10731
 Dodds-Eden, K., Gillessen, S., Fritz, T. K., et al. 2011, *ApJ*, 728, 37
 Dodds-Eden, K., Porquet, D., Trap, G., et al. 2009, *ApJ*, 698, 676
 Doeleman, S. S., Weintraub, J., Rogers, A. E. E., et al. 2008, *Natur*, 455, 78
 Dolence, J. C., Gammie, C. F., Shiokawa, H., & Noble, S. C. 2012, *ApJL*, 746, L10
 Eckart, A., Baganoff, F. K., Zamaninasab, M., et al. 2008, *A&A*, 479, 625
 Event Horizon Telescope Collaboration, Akiyama, K., Alberdi, A., et al. 2019a, *ApJL*, 875, L1
 Event Horizon Telescope Collaboration, Akiyama, K., Alberdi, A., et al. 2019b, *ApJL*, 875, L5
 Fazio, G. G., Hora, J. L., Witzel, G., et al. 2018, *ApJ*, 864, 58
 Fruscione, A., McDowell, J. C., Allen, G. E., et al. 2006, *Proc. SPIE*, 6270, 62701V
 Genzel, R., Eisenhauer, F., & Gillessen, S. 2010, *RvMP*, 82, 3121
 Ghez, A. M., Salim, S., Weinberg, N. N., et al. 2008, *ApJ*, 689, 1044
 Gillessen, S., Eisenhauer, F., Fritz, T. K., et al. 2009, *ApJL*, 707, L114
 Gillessen, S., Genzel, R., Fritz, T. K., et al. 2012, *Natur*, 481, 51
 Gillessen, S., Plewa, P. M., Eisenhauer, F., et al. 2017, *ApJ*, 837, 30
 Goldwurm, A., Brion, E., Goldoni, P., et al. 2003, *ApJ*, 584, 751
 Gravity Collaboration, Abuter, R., Amorim, A., et al. 2018a, *A&A*, 618, L10
 Gravity Collaboration, Abuter, R., Amorim, A., et al. 2018b, *A&A*, 615, L15
 Gravity Collaboration, Abuter, R., Amorim, A., et al. 2019, *A&A*, 625, L10
 Hornstein, S. D., Matthews, K., Ghez, A. M., et al. 2007, *ApJ*, 667, 900
 Houck, J. C., & Denicola, L. A. 2000, in ASP Conf. Ser. 216, *Astronomical Data Analysis Software and Systems IX*, ed. N. Manset, C. Veillet, & D. Crabtree (San Francisco, CA: ASP), 591
 Jin, C., Ponti, G., Haberl, F., & Smith, R. 2017, *MNRAS*, 468, 2532
 Karssen, G. D., Bursa, M., Eckart, A., et al. 2017, *MNRAS*, 472, 4422
 Kennea, J. A., Burrows, D. N., Kouveliotou, C., et al. 2013, *ApJL*, 770, L24
 Kostić, U., Čadež, A., Calvani, M., & Gomboc, A. 2009, *A&A*, 496, 307
 Leahy, D. A., Darbro, W., Elsner, R. F., et al. 1983, *ApJ*, 266, 160
 Liu, S., & Melia, F. 2002, *ApJL*, 566, L77
 Liu, S., Petrosian, V., & Melia, F. 2004, *ApJL*, 611, L101
 Markoff, S., Falcke, H., Yuan, F., & Biermann, P. L. 2001, *A&A*, 379, L13
 Mauerhan, J. C., Morris, M., Walter, F., & Baganoff, F. K. 2005, *ApJL*, 623, L25
 Melia, F. 1992, *ApJL*, 387, L25

- Meyer, L., Do, T., Ghez, A., et al. 2008, *ApJL*, 688, L17
- Mori, K., Gotthelf, E. V., Zhang, S., et al. 2013, *ApJL*, 770, L23
- Mościbrodzka, M., Gammie, C. F., Dolence, J. C., Shiokawa, H., & Leung, P. K. 2009, *ApJ*, 706, 497
- Mossoux, E., & Grosso, N. 2017, *A&A*, 604, A85
- Mossoux, E., Grosso, N., Bushouse, H., et al. 2016, *A&A*, 589, A116
- Mossoux, E., Grosso, N., Vincent, F. H., & Porquet, D. 2015, *A&A*, 573, A46
- Neilsen, J., Markoff, S., Nowak, M. A., et al. 2015, *ApJ*, 799, 199
- Neilsen, J., Nowak, M. A., Gammie, C., et al. 2013, *ApJ*, 774, 42
- Nowak, M. A., Neilsen, J., Markoff, S. B., et al. 2012, *ApJ*, 759, 95
- Park, T., Kashyap, V. L., Siemiginowska, A., et al. 2006, *ApJ*, 652, 610
- Plewa, P. M., Gillessen, S., Pfuhl, O., et al. 2017, *ApJ*, 840, 50
- Ponti, G., De Marco, B., Morris, M. R., et al. 2015, *MNRAS*, 454, 1525
- Ponti, G., George, E., Scaringi, S., et al. 2017, *MNRAS*, 468, 2447
- Porquet, D., Grosso, N., Predehl, P., et al. 2008, *A&A*, 488, 549
- Porquet, D., Predehl, P., Aschenbach, B., et al. 2003, *A&A*, 407, L17
- Quataert, E. 2002, *ApJ*, 575, 855
- Rea, N., Esposito, P., Pons, J. A., et al. 2013, *ApJL*, 775, L34
- Reid, M. J., & Brunthaler, A. 2004, *ApJ*, 616, 872
- Russell, C. M. P., Wang, Q. D., & Cuadra, J. 2017, *MNRAS*, 464, 4958
- Scargle, J. D. 1982, *ApJ*, 263, 835
- Smith, R. K., Valencic, L. A., & Corrales, L. 2016, *ApJ*, 818, 143
- Timmer, J., & Koenig, M. 1995, *A&A*, 300, 707
- Verner, D. A., Ferland, G. J., Korista, K. T., & Yakovlev, D. G. 1996, *ApJ*, 465, 487
- Wang, Q. D., Nowak, M. A., Markoff, S. B., et al. 2013, *Sci*, 341, 981
- Wilms, J., Allen, A., & McCray, R. 2000, *ApJ*, 542, 914
- Witzel, G., Eckart, A., Bremer, M., et al. 2012, *ApJS*, 203, 18
- Witzel, G., Martinez, G., Hora, J., et al. 2018, *ApJ*, 863, 15
- Witzel, G., Sitarski, B. N., Ghez, A. M., et al. 2017, *ApJ*, 847, 80
- Xu, Y.-D., Narayan, R., Quataert, E., Yuan, F., & Baganoff, F. K. 2006, *ApJ*, 640, 319
- Yuan, F., & Narayan, R. 2004, *ApJ*, 612, 724
- Yuan, F., Quataert, E., & Narayan, R. 2003, *ApJ*, 598, 301
- Yuan, Q., & Wang, Q. D. 2016, *MNRAS*, 456, 1438
- Yusef-Zadeh, F., Bushouse, H., Dowell, C. D., et al. 2006, *ApJ*, 644, 198
- Yusef-Zadeh, F., Wardle, M., Dodds-Eden, K., et al. 2012, *AJ*, 144, 1
- Yusef-Zadeh, F., Wardle, M., Schödel, R., et al. 2016, *ApJ*, 819, 60
- Zhang, S., Baganoff, F. K., Ponti, G., et al. 2017, *ApJ*, 843, 96
- Zubovas, K., Nayakshin, S., & Markoff, S. 2012, *MNRAS*, 421, 1315